

Dissecting the nanoHz gravitational wave sky: frequency-correlated anisotropy induced by eccentric supermassive black hole binaries.

B. E. Moreschi,^{1,2,3,*} S. Valtolina,^{4,5} A. Sesana,¹ G. Shaifullah,^{1,2,3} M. Falxa,¹ L. Speri,⁶ D. Izquierdo-Villalba,^{1,2} and A. Chalumeau⁷

¹ Dipartimento di Fisica “G. Occhialini”, Università degli Studi di Milano-Bicocca, Piazza della Scienza 3, I-20126 Milano, Italy

² INFN, Sezione di Milano-Bicocca, Piazza della Scienza 3, I-20126 Milano, Italy

³ INAF – Osservatorio Astronomico di Cagliari, Via della Scienza 5, I-09047 Selargius (CA), Italy

⁴ Max Planck Institute for Gravitational Physics (Albert Einstein Institute), Callinstrasse 38, D-30167 Hannover, Germany

⁵ Leibniz Universität Hannover, Callinstrasse 38, D-30167 Hannover, Germany

⁶ European Space Agency (ESA), European Space Research and Technology Centre (ESTEC), Keplerlaan 1, 2201 AZ Noordwijk, the Netherlands

⁷ ASTRON, Netherlands Institute for Radio Astronomy, Oude Hoogeveensedijk 4, 7991 PD, Dwingeloo, The Netherlands

Received xxxx; accepted xxxx

ABSTRACT

Revealing the nature of the nanoHz gravitational wave (GW) signal recently reported by Pulsar Timing Arrays (PTAs) collaborations around the world is the next goal of low-frequency GW astronomy. The signal likely originates from the incoherent superposition of GWs emitted by a cosmological population of supermassive black hole binaries (SMBHBs). Those binaries can be highly eccentric and/or strongly coupled to their nuclear environment, resulting in an attenuation of the overall GW signal at low frequencies. In this paper, we propose to use the correlation properties of the distributed GW power in the sky across the frequency spectrum as a smoking gun for eccentric SMBHBs thus allowing to break the spectral degeneracy between eccentricity and environmental effect. The simple underlying idea is that, contrary to circular binaries, eccentric ones emit a broadband spectrum thus resulting in similar sky maps at different frequencies. We first demonstrate the applicability of this simple concept on sky maps constructed directly from the theoretical sky distribution of the GWB power induced by realistic populations of SMBHBs. We then demonstrate the viability of this analysis on simulated SKA-like PTA data. By statistically comparing sky maps reconstructed from hundreds injected circular and highly eccentric SMBHB populations, we find that eccentricity can be detected at 3σ in more than 50% of cases.

Key words. gravitational waves - pulsars - pulsar timing array - black holes - GWB - anisotropy - methods: data analysis.

1. Introduction

The increasingly stronger evidence for a gravitational wave background (GWB) in Pulsar Timing Array (PTA) experiments has intrigued the scientific community worldwide. Multiple regional PTA collaborations have reported different levels of confidence for the evidence of a common low-frequency signal in their latest data releases (Antoniadis et al. 2023; Xu et al. 2023; Agazie et al. 2023b; Reardon et al. 2023; Miles et al. 2024), which shows cross-pulsar correlation properties compatible with the ones expected for a stochastic GWB (Hellings & Downs 1983). Adding more pulsars with longer observation time spans will soon bring PTA experiments to the sensitivity required for robust astrophysical inference about the nature of the low-frequency gravitational wave (GW) sources.

In short, PTA experiments study the nano-Hertz (nHz) frequency range, where the dominant signal is expected to be a stochastic GWB. This signal affects the time of arrivals (ToAs) of pulsar observations as a low-frequency noise that is spatially correlated between different pulsars, as predicted by the Hellings and Downs (HD) correlation function (Hellings & Downs 1983).

The GWB can be generated by the superposition of periodic GWs emitted by a cosmic population of supermassive black hole binaries (SMBHBs, Rajagopal & Romani 1995; Jaffe & Backer 2003; Wyithe & Loeb 2003; Sesana et al. 2008; Rosado et al. 2015). Although it could arise from a variety of cosmological phenomena such as: cosmic strings networks (Damour & Vilenkin 2000), non-standard inflationary scenario breaking the slow-roll consistency relations (Bartolo et al. 2007; Boyle & Buonanno 2008; Sorbo 2011), cosmic domain walls (Hiramatsu et al. 2014), primordial curvature perturbations (Tomita 1967; Matarrese et al. 1993) or even QCD phase transitions (Kosowsky et al. 1992; Hindmarsh et al. 2014). In this article, we work under the assumption that the sought GWB signal is produced by a population of SMBHBs and study how the discrete nature of the GW spectrum produced by this population leads to measurable anisotropies, provided a sufficiently sensitive PTA.

Standard search pipelines used in PTA analysis (Ellis et al. 2019) model the GWB as a Gaussian, isotropic, stationary process characterized by a power spectral density (PSD) well modeled by a powerlaw. Such a description for the GW spectrum is well justified for an idealized population of circular binaries uniformly distributed over the sky (Sesana et al. 2008).

* e-mail: b.moreschi1@campus.unimib.it

However, none of these statistical properties are expected to accurately describe the GWB signal produced by a realistic SMBHB population. Finite number statistics, environmental effects such as gas and stellar hardening, and eccentricity are expected to produce significant deviations of the spectra from the smooth powerlaw approximation (Sesana et al. 2008; Ravi et al. 2014; Sampson et al. 2015; Bécsy et al. 2023; Valtolina et al. 2024). Moreover, the discreteness of the SMBHB population and/or strong individual sources may produce extra power at specific frequencies, also resulting in highly anisotropic and non-Gaussian signals (Sesana et al. 2009; Ravi et al. 2012; Kelley et al. 2017; Ferranti et al. 2025; Bécsy et al. 2025). Further, the eccentricity of SMBHBs might break the assumption of stationarity (Sesana 2013; Falxa et al. 2024). Finally, resolving individual sources remains a high priority target for PTAs (Agazie et al. 2023; Antoniadis et al. 2024; Miles et al. 2024), with some suggestions that the observed nHz GWB-sky already has some degree of anisotropy (Grunthal et al. 2024).

One of the key elements to distinguish between a cosmological GWB and an astrophysical background is the expected presence of anisotropic features. While cosmological signals are anticipated to be isotropic (within Gaussian oscillations), the discrete nature of a population of astrophysical SMBHBs, combined with galaxy clustering effects, may produce detectable overdensities of GW power. Cosmic microwave background (CMB) analysis techniques have been adapted to the PTA scenario to model these anisotropic features (Ölmez et al. 2012; Mingarelli et al. 2013; Gair et al. 2014; Rosado et al. 2015). The idea is to model the GW power as a function of the sky location; this can be done using different bases, where the most common ones are the pixel basis, the spherical harmonics basis and the square-root spherical harmonics basis (Mingarelli et al. 2017; Taylor et al. 2020). Applications of these techniques to real PTA datasets have been carried out by the PTA collaborations without assessing any definitive result in favor of an anisotropic GWB model over an isotropic model (Taylor & Gair 2013; Taylor et al. 2015; Agazie et al. 2023a; Grunthal et al. 2024).

Besides discriminating between cosmological and astrophysical origin, the measured degree of anisotropy can also be used to constrain the properties of the emitting GW sources.

While Pol et al. (2022) and Depta et al. (2024) assess the sensitivity of a PTA dataset to anisotropic features of a GWB signal, many studies have investigated the relation between different astrophysical models for galaxy clustering evolution and SMBHB formation and the results of PTA anisotropy studies, using both analytical predictions (Sato-Polito & Kamionkowski 2023; Allen et al. 2024; Grimm et al. 2025; Cusin et al. 2025) and numerical simulations (Gardiner et al. 2024; Lemke et al. 2024; Sah et al. 2024; Semenzato et al. 2024).

In this paper, we explore the possibility of using anisotropy to discriminate between SMBHB populations affected by strong environmental effects and SMBHB populations featuring binaries with significant eccentricity.

Both eccentricity and environmental effects are expected to absorb some of the GW power at the lowest frequencies, making the PSD of the GWB deviate significantly from the powerlaw model (Sesana 2013; Ravi et al. 2014). Thus, from the shape of the PSD only it can be extremely hard (if at all possible) to distinguish between the two scenarios. Here, we introduce a possible strategy to discriminate between them based on the different imprints they leave in the GWB anisotropy as a function of frequency. The basic underlying idea is that circular GW sources emit monochromatically with a frequency equal to twice their orbital frequency. Therefore, sky maps reconstructed at different

frequencies will feature uncorrelated anisotropies, due to different binaries being dominant in each sky map. Conversely, eccentric binaries emit GWs over many harmonics, which is expected to induce some level of correlation between sky maps of GW power at different frequencies. In other words, the same source will be detectable in more than one sky map. To implement and test this idea, from the spherical harmonic decomposition of the GWB signal, we reconstruct the sky map of GW power at different frequencies (Mingarelli et al. 2013; Gair et al. 2014), and then compute their correlation.

The idea of cross-correlating sky maps has been recently explored in Semenzato et al. (2024) and Cusin et al. (2025) to quantify the relation between the GWB sky power distribution and galaxy large-scale structures. Our approach is different in the sense that we are decomposing the nHz GW signal into several sky maps at different frequencies and computing their cross-correlation. In practice, the GW signal is cross-correlated with itself rather than with the distribution of galaxies and large-scale structures in the sky. As we were completing this work, Sah et al. (2025) presented an independent, parallel investigation that touches on a few of the points examined here. In this article, besides showing the theoretical idea, we go a step further by testing our methodology using state-of-the-art SMBHB catalog realizations injected in realistic PTA simulated datasets.

The paper is structured as follows. In Section 2, we describe the tools upon which our analysis is built, including techniques to decompose and cross-correlate sky maps and models used to generate the SMBHB populations. In Section 3 we present the key concept of cross-correlating GW power at different frequencies to detect eccentricity on theoretical GW power distributions obtained from the theoretical SMBHB populations. In Section 4 we carry out a more realistic experiment by injecting the GW signal in an idealized PTA. We describe our PTA simulation approach, define the detection statistics involved in the analysis and present the main results. Finally, in Section 5 we comment on the merits and limitations of our investigation, and we point to future directions for further development of this analysis technique.

2. Analysis methods

In this section, we present the main ingredients of our analysis, including strategies to decompose and cross-correlate different sky maps, as well as models adopted to simulate the SMBHB populations we are considering.

2.1. Construction and correlation of GW power sky maps

A way to distinguish eccentric and quasi-circular populations is by inspecting and correlating the distribution of the GWB power across the sky at different frequency bins. Supposing that we evaluate the GW signal over an array of discrete frequency bins f_j , the GWB PSD at each frequency is written as:

$$S_h(f_j) = \frac{h_c^2(f_j)}{12\pi^2 f_j^3} \quad (1)$$

where $h_c(f_j)$ is the characteristic strain of the GW signal, which we will introduce in Section 3.1. At each f_j , the GWB PSD can be factorized as:

$$S'_h(\hat{\Omega}, f_j) = S_h(f_j) \frac{P(\hat{\Omega}, f_j)}{4\pi} \quad (2)$$

where $S_h(f_j)$ describes the spectral content of the GWB, and $P(\hat{\Omega}, f_j)$ is the distribution of the GWB power in the sky such that

$\int d\hat{\Omega} P(\hat{\Omega}, f_j) = 4\pi \forall f_j$. It is possible to decompose the GWB power using either the spherical harmonics or the square-root spherical harmonics bases¹. With the former method, we write (Taylor et al. 2015):

$$P_{\text{spha}}(\hat{\Omega}, f_j) = \sum_{\ell=0}^{\infty} \sum_{m=-\ell}^{\ell} a_{\ell m}(f_j) Y_{\ell m}(\hat{\Omega}) \quad (3)$$

where $Y_{\ell m}$ are the real valued spherical harmonics with coefficients $a_{\ell m}$.

The number of l -multipoles that can be resolved by a PTA is limited by the number of observed pulsars such that $l_{\text{max}} \lesssim \sqrt{N_{\text{psrs}}}$ (Romano & Cornish 2017). Since we simulate 200 pulsars (as described in Section 4), we set $l_{\text{max}} = 10$ ², and the sky map resolution $N_{\text{side}} = 8$.

Since the spherical harmonics decomposition allows negative GWB power, which is unphysical, we can use as an alternative method the square root spherical harmonic basis proposed in Taylor et al. (2020), so that we can write the GWB power as:

$$P_{\text{sqr}}(\hat{\Omega}, f_j)^{1/2} = \sum_{L=0}^{\infty} \sum_{M=-L}^L b_{LM}(f_j) Y_{LM}(\hat{\Omega}) \quad (4)$$

where Y_{LM} are the real valued spherical harmonics and b_{LM} are coefficients of the square-root decomposition, related to $a_{\ell m}$ as:

$$a_{\ell m} = \sum_{LM} \sum_{L'M'} b_{LM} b_{L'M'} \beta_{\ell m}^{LM, L'M'}, \quad (5)$$

where we omit the f_j index for brevity of notation, and:

$$\beta_{\ell m}^{LM, L'M'} = \sqrt{\frac{(2L+1)(2L'+1)}{4\pi(2\ell+1)}} C_{LM, L'M'}^{\ell m} C_{L0, L'0}^{\ell 0} \quad (6)$$

and $C_{LM, L'M'}^{\ell m}$ are the Clebsch-Gordan coefficients. Thus, using square root spherical harmonics we decompose $P_{\text{sqr}}(\hat{\Omega}, f_j)^{1/2}$ instead of $P_{\text{spha}}(\hat{\Omega}, f_j)$ so that the GWB power is always positive.

Once the j -th map is decomposed into spherical harmonics, we compute the C_{ℓ} coefficients of its ℓ mode decomposition, representing the GWB power distribution across different angular scales corresponding to $\theta = 180^\circ/\ell$:

$$C_{\ell}^{j\text{-map}} = \frac{1}{2\ell+1} \sum_{m=-\ell}^{\ell} |a_{\ell m}^j|^2. \quad (7)$$

We then compute the cross-correlation of each C_{ℓ} between maps i and j as:

$$C_{\ell}^i C_{\ell}^j = \frac{1}{2\ell+1} \sum_{m=-\ell}^{\ell} a_{\ell m}^i (a_{\ell m}^j)^*. \quad (8)$$

Finally, we introduce the normalized correlation coefficient between the two maps r_{ℓ}^{ij} :

$$r_{\ell}^{ij} = \frac{C_{\ell}^i C_{\ell}^j}{\sqrt{C_{\ell}^i C_{\ell}^j}}, \quad (9)$$

and a global weighted correlation \bar{r}^{ij} defined as:

$$\bar{r}^{ij} = \frac{\sum_{\ell=0}^{\ell_{\text{max}}} (2\ell+1) r_{\ell}^{ij}}{\sum_{\ell=0}^{\ell_{\text{max}}} (2\ell+1)}, \quad (10)$$

thus taking into account all values of ℓ and m . \bar{r}^{ij} is normalized such that it assumes values between $[-1, +1]$. Note that, although the procedure to evaluate the correlation \bar{r}^{ij} only requires the $a_{\ell m}$ coefficients, we introduced in Eq. (4) also the square-root basis decomposition because in the realistic experiment carried in Section 4 we will use this basis to construct sky maps using the frequentist approach described in Pol et al. (2022). We will then decompose this map in standard spherical harmonics according to Eq. (3) and proceed with the computation of the correlation.

Values of \bar{r}^{ij} near +1 or -1 indicate a strong correlation or anti-correlation, while values near zero imply no correlation between maps. In our specific problem, the expectation is that $\bar{r} \approx 1$ when correlating sky maps produced by populations of eccentric SMBHBs, since eccentric bright sources emit in multiple harmonics. Conversely, we anticipate $\bar{r} \approx 0$ if we correlate sky maps of quasi-circular populations since different sky maps are dominated by distinct quasi-monochromatic³ binaries.

2.2. SMBHB populations

In order to study the possibility of discriminating between eccentric and quasi-circular binaries subjected to environmental effects, we need to construct cosmic populations of SMBHBs that feature both. We therefore need a model for the cosmic SMBHB merger rate and for the dynamical evolution of individual binary systems.

For the cosmic SMBHB merger rate, we consider one of the observation-based models constructed in Sesana (2013); Rosado et al. (2015). In short, the SMBH merger rate is anchored to the parent galaxy merger rate, assuming a SMBH-host galaxy relation from the literature. The host galaxy merger rate is instead constructed by multiplying the redshift-dependent galaxy mass function by the galaxy pair fraction and dividing it by an estimated merger timescale of the pairs. The mass function and pair fractions are directly measured from observations and taken from Tomczak et al. (2014) and Bundy et al. (2009) respectively. Conversely, the merger timescales are measured from simulations and we use estimates from Lotz et al. (2010). Finally, the galaxy merger rate is converted to a SMBHB merger rate using the observed $M_{\text{BH}} - M_{\text{bulge}}$ relation of Kormendy & Ho (2013), thus obtaining the MBHB merger density dn per unit primary MBH mass M_1 , mass ratio q and cosmic source frame time t_r : $d^3n/(dt_r dM_1 dq)$. One can then write $n = dN/dV_c$ and multiply by the comoving volume shell dV_c/dz and by the time spent by a source at each rest-frame Keplerian log-frequency $dt_r/d\ln f_{K,r}$ to obtain the number of SMBHBs emitting per unit mass, mass-ratio, redshift and rest frame frequency: $d^4N/(dz dM_1 dq d\ln f_{K,r})$.

It is in this last step that the SMBHB dynamics kick in. In fact, the binary frequency evolution $df_{K,r}/dt_r$ is driven both by the interaction with the environment and GW backreaction, and depends on the eccentricity (which we have ignored thus far). If we assume that SMBHB hardening proceeds by scattering of

¹ While the choice of basis can be arbitrary, these are the two most common in literature.

² Setting $l_{\text{max}} = 10$ gives us a sky resolution $\theta = 180 \text{ deg} / l = 18 \text{ deg}$.

³ In our 'circular' population, binaries are in fact quasi-circular (generally eccentricity $e < 0.1$) due to realistic evolution via three body scattering. Their GW emission is therefore not strictly monochromatic but it is nonetheless overwhelmingly dominated by a single GW harmonic (at twice the binary orbital frequency).

background stars, we can write the evolution for $f_{K,r}$ and e as (Truant et al. 2025):

$$\frac{df_{K,r}}{dt_r} = \left(\frac{df_{K,r}}{dt_r} \right)_* + \left(\frac{df_{K,r}}{dt_r} \right)_{\text{GW}} = \frac{3G^{4/3}M^{1/3}H\rho}{2(2\pi)^{2/3}\sigma} f_{K,r}^{1/3} + \frac{96(GM)^{5/3}}{5c^5} (2\pi)^{8/3} f_{K,r}^{11/3} \mathcal{F}(e), \quad (11)$$

$$\frac{de}{dt_r} = \left(\frac{de}{dt_r} \right)_* + \left(\frac{de}{dt_r} \right)_{\text{GW}} = \frac{G^{4/3}M^{1/3}\rho HK}{(2\pi)^{2/3}\sigma} f_{K,r}^{-2/3} - \frac{(GM)^{5/3}}{15c^5} (2\pi f_{K,r})^{8/3} \mathcal{G}(e), \quad (12)$$

where M and \mathcal{M} are the SMBHB total mass and chirp mass respectively, σ and ρ are the velocity dispersion and stellar density of the host galaxy at the binary influence radius, H and K are dimensionless parameters calibrated against three-body scattering experiments (Sesana et al. 2006), and the subscripts $*$ and GW denote the stellar hardening and GW backreaction components. Here $\mathcal{F}(e)$ and $\mathcal{G}(e)$ take the form:

$$\mathcal{F}(e) = \frac{1 + (73/24)e^2 + (37/96)e^4}{(1 - e)^{7/2}},$$

$$\mathcal{G}(e) = \frac{304e + 121e^3}{(1 - e^2)^{5/2}}. \quad (13)$$

To complete the dynamical evolution model, we need to specify ρ , σ , and an initial eccentricity e_0 at a given initial orbital frequency f_0 . For each binary mass, the fiducial values of ρ , σ , and f_0 are computed following the procedure described in Sesana (2010), and we assume that all binaries share the same eccentricity at formation $e_0(f_0)$. Note that each binary evolves from f_0 , e_0 via the coupled differential Eqs. (11) and (12). Therefore, any binary observed at a frequency $f_{K,r}$ has an eccentricity $e(e_0, f_0, f)$ which is uniquely set by this evolution. We can therefore characterize the final distribution of observed SMBHBs emitting GWs in the nHz band as: $d^5N/(dz dM_1 dq d\ln f_{K,r} de)$.

3. Expected GWB anisotropy signature

In this section, we infer the astrophysical properties of different SMBHB populations, investigating the expected anisotropic GWB signatures. For this, we computed the expected weighted correlation \bar{r}^{ij} , presented in Section 2.1, given the theoretical h_c^2 distribution across the sky generated by a SMBHB population.

3.1. Theoretical computation of the GWB strain

Given the differential population of SMBHBs described in the previous section, the characteristic strain $h_c(f)$ of the overall emitted GW signal can be written as:

$$h_c^2(f) = \int_0^\infty dz \int_0^\infty dM_1 \int_0^1 dq \int_0^1 de \frac{d^5N}{dz dM_1 dq d\ln f_{K,r} de} \times h^2(f_{K,r}) \sum_{n=1}^{+\infty} \frac{g(n, e)}{(n/2)^2} \Big|_{f_{K,r}=f(1+z)/n}, \quad (14)$$

where

$$h(f_{K,r}) = \sqrt{\frac{32}{5} \frac{(GM)^{5/3}}{c^4 D}} (2\pi f_{K,r})^{4/3}, \quad (15)$$

Article number, page 4 of 12

| Settings | Pop 1 | Pop 2 |
|---------------------------------|------------------|-------------|
| Eccentricity at formation e_0 | 0.01 | 0.9 |
| Density of the environment | $\rho \times 10$ | $\rho / 10$ |

Table 1: Astrophysical properties of the populations used in the analysis. ρ is the fiducial stellar density at influence radius as estimated in Sesana (2010).

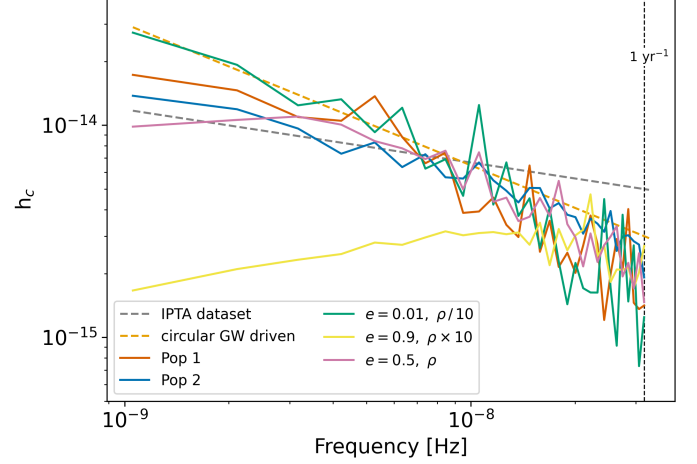


Fig. 1: Characteristic strain as a function of the frequency for different SMBHB populations. The dashed orange line is the GWB signal produced by a circular, GW-driven population, with $f^{-2/3}$. The dashed dark gray line is the mean GWB powerlaw recovered using a factorised likelihood analysis of three PTA collaboration data (Agazie et al. 2024). The parameters of eccentricity e_0 and fiducial stellar density ρ at influence radius for Pop 1 and 2 are reported in Table 1, alternative models featuring variations of these parameters are also shown.

and D is the source comoving distance. In practice, each source contributes through an infinite series of n harmonics of the orbital frequency $f_{K,r}$, adjusted by $1 + z$ to account for cosmological redshift and thus observed at frequency $f = n f_{K,r} / (1 + z)$. Each harmonic is weighted by a function that depends on e :

$$g(n, e) = \frac{n^4}{32} \left[\left(J_{n-2}(ne) - 2eJ_{n-1}(ne) + \frac{2}{n}J_n(ne) + 2eJ_{n+1}(ne) - J_{n+2}(ne) \right)^2 + (1 - e^2) \left(J_{n-2}(ne) - 2J_n(ne) + J_{n+2}(ne) \right)^2 + \frac{4}{3n^2} J_n^2(ne) \right], \quad (16)$$

where J_n is the n -th order Bessel function of the first kind (Peters & Mathews 1963).

Eq. (14) is the continuum limit solution of an inherently discrete problem. In fact the GWB is made of a discrete population of SMBHB and PTAs observe for a finite amount of time T and hence have a resolution limit $\Delta f = 1/T$. This means that the GWB spectrum is evaluated in discrete frequency bins $\Delta f_j = [j/T, (j+1)/T]$, centered at $f_j = (2j+1)/(2T)$ for $j = 1, \dots, N_b$, being N_b the number of considered frequency bins. Throughout this paper we assume $T = 30$ yrs. Therefore, in a real-life experiment, Eq. (14) takes the form (Amaro-Seoane

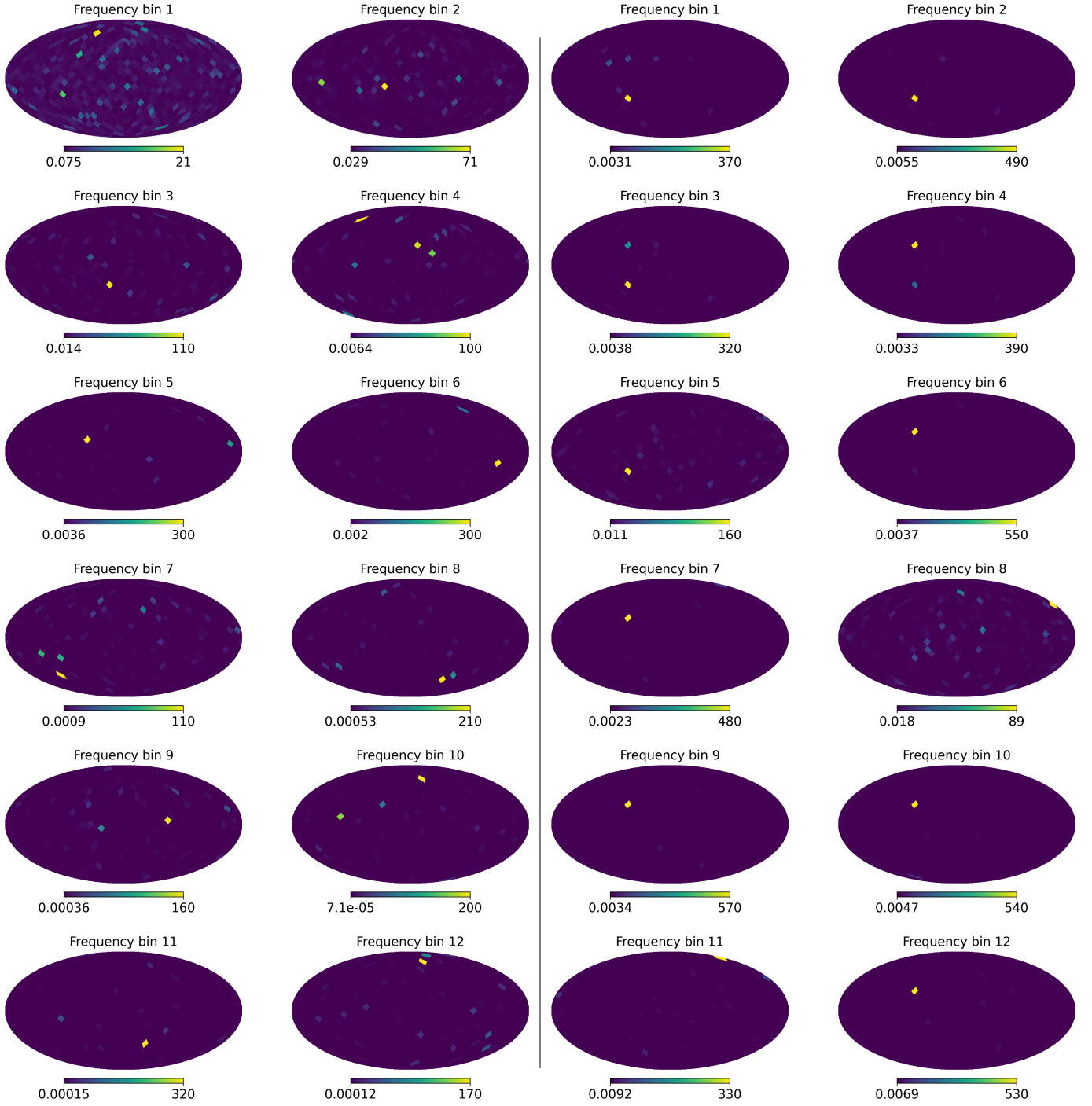


Fig. 2: Sky maps of the GWB power distribution $P(\hat{\Omega}_k, f_j)$ in the first 12 frequency bins of Pop 1 (left plot) and Pop 2 (right plot). We notice that maps are often dominated by a single bright source, visible as a yellow pixel. For a quasi-circular population, different maps show bright sources located at different sky locations. On the other hand, when considering an eccentric population, the same bright source appears at the same sky location across multiple maps.

et al. 2010):

$$h_c^2(f_j) = \sum_{i=1}^N \sum_{n=1}^{+\infty} h_i^2(f_{K,r_i}) \frac{g(n, e_i)}{(n/2)^2} \frac{n f_{K,r_i}}{\Delta f (1+z)} \Theta\left(\frac{n f_{K,r_i}}{1+z}, \Delta f_j\right), \quad (17)$$

where $\Theta = 1$ if $n f_{K,r_i}/(1+z) \in \Delta f_j$, and $\Theta = 0$ otherwise. Here the first sum is over the N SMBHBs composing the population, each of which contributes to the signal with n harmonics. Note that in the continuum limit, for a population of circular

GW driven binaries, Eqs. (17) and (14) tend to the well known power-law $h_c(f) = A_{\text{GWB}}(f/1\text{yr}^{-1})^{-2/3}$, where A_{GWB} is the nominal GWB amplitude at $f = 1\text{yr}^{-1}$ (Phinney 2001). The SMBHB population described in Section 2.2 results in $A_{\text{GWB}} \sim 3 \times 10^{-15}$, consistent with current PTA observations.

As proof of concept, we investigate two models sharing the same SMBHB merger rate but differing in the dynamical evolution because of different e_0 and ρ as detailed in Table 1. We refer to the models as Pop 1, and Pop 2. For each

model we draw 100 Monte Carlo realizations of the distribution $d^5N/(dz dM_1 dq d\ln f_{K,r} de)$. For each sampled source we extract the rest frame masses, redshift, observed GW second harmonic, eccentricity and the h_c^2 contributed at each frequency bin, constructing the GWB strain amplitude according to Eq. (17).

The result of this procedure is shown in Figure 1 for selected realizations of the two models. There, the red and blue curves correspond to Pop 1 and Pop 2, respectively. The other solid lines show backgrounds generated by populations with different initial conditions. We notice some deviations in the background slope at low frequencies with respect to a GWB generated by a population of circular, GW-driven SMBHBs (dashed orange line). A similar flat slope has been reported by IPTA (Agazie et al. 2024, dashed dark gray line). Any deviation from the powerlaw is due to the discrete nature of the GWs emitted by these SMBHBs, which produces a structured GWB (Sesana et al. 2008), as well as the level of environmental effects and the eccentricity of the sources that suppress the power at low-frequencies, as mentioned before. In fact, SMBHBs influenced by stellar hardening evolve faster and spend less time emitting GWs at lower frequencies. On the other hand, eccentric SMBHBs emit GWs at multiple harmonics of the orbital frequency, distributing the GW power at higher frequencies. Although the two populations have different values of e_0 and different strengths of environmental coupling, it is not possible to distinguish the nature of the population from their spectra alone. This is why we investigate a new method which can be applied to real PTAs datasets to determine whether the measured flat slope is due to some level of eccentricity or environmental effects (or a combination of both, although we defer this latter case to future work).

3.2. Cross-correlation results

To map the sky distribution of the GWB power, we assign to the i -th SMBHB a random sky location $\hat{\Omega}_i$, we divide the sky in pixels $\hat{\Omega}_k$ of equal area $\Delta\Omega$ and evaluate the discrete version $P(\hat{\Omega}_k, f_j)$ of the power distribution in Eq. (2) as

$$P(\hat{\Omega}_k, f_j) = \frac{h_c^2(\hat{\Omega}_k, f_j)}{h_c^2(f_j)}, \quad (18)$$

where $h_c^2(\hat{\Omega}_k, f_j)$ is evaluated by multiplying Eq. (17) by $\delta(\hat{\Omega}_i, \hat{\Omega}_k)$, thus counting in each pixel only those SMBHBs falling within it.

The distribution of $P(\hat{\Omega}_k, f_j)$ across the sky is shown in Figure 2 for the first 12 frequency bins of two selected realizations of both models (Pop 1 and Pop 2). The figure demonstrates the difference between quasi-circular and eccentric populations when it comes to the sky distribution of the GW power as a function of frequency. We constructed these sky maps using HEALPY (Zonca et al. 2019) and plotted the GWB power in equal-area pixels, where $N_{\text{pix}} = 12N_{\text{side}}^2$. We used $N_{\text{side}}=8$ due to limitations from the number of pulsars in the PTA, as discussed above.

We distributed the sources randomly on the sky, leaving the study of potential anisotropies due to galaxy clustering for future work. For the eccentric population (Pop 2, right plot) we observe the contribution of the same source, at a specific position in the sky, emitting GWs across multiple harmonics as per Eq. (16), and thus in different (frequency bin-wise) sky maps. For this specific realization, we clearly see one source dominating in bins 1, 2, 3 and 5, and another source dominating in bins 4, 6, 7, 9, 10 and 12. It is therefore possible to note the same power distribution pattern in nearby frequency bins, and we expect a certain degree of correlation in the resulting sky maps.

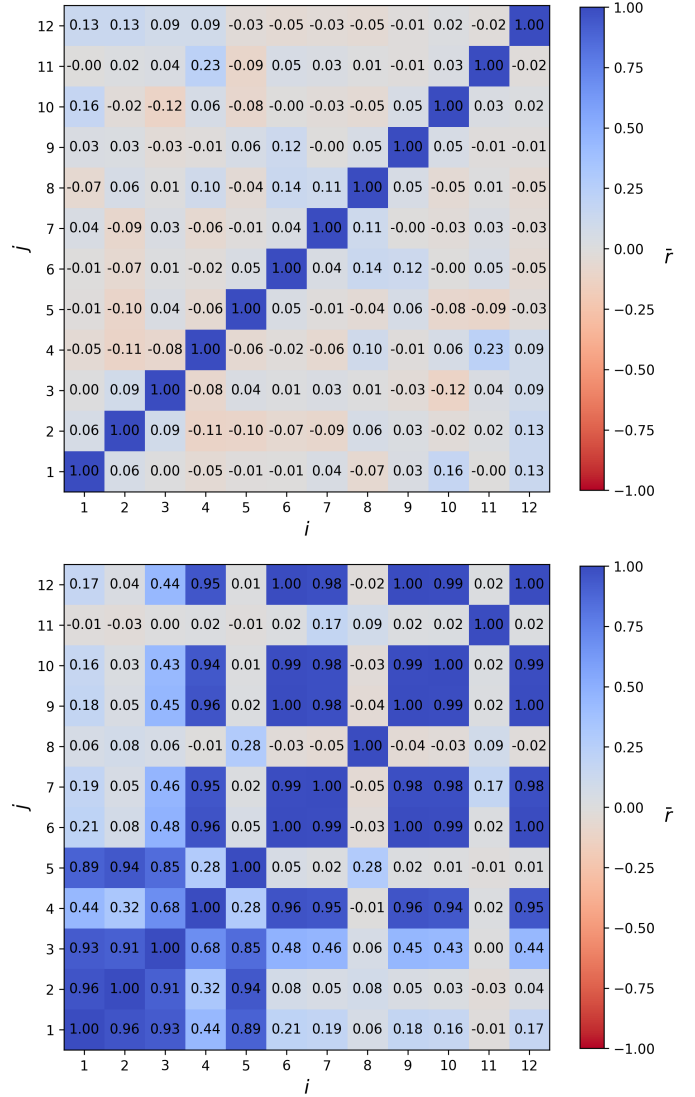


Fig. 3: Weighted correlation \bar{r}^{ij} from a single realization of Pop 1 (top panel) and Pop 2 (bottom panel). The color scale tracks the \bar{r}^{ij} values, which are also reported in each cell of the matrix. The i and j indices correspond to different frequency bins.

Conversely, quasi-circular binaries (Pop 1, left plot) subjected to environmental effects cannot produce this kind of recursive patterns, and we do not expect the GW power between different sky maps to be correlated. This indicates that correlation across sky maps can be used to break the degeneracy of the spectrum that we saw in Figure 1.

To evaluate the correlation between sky maps at different frequencies \bar{r}^{ij} , we decompose the power $P(\hat{\Omega}_k, f_j)$ in spherical harmonics according to Eq. (3) and follow the procedure presented in Section 2.1. We evaluate \bar{r}^{ij} across the 12 lowest frequency bins, thus constructing a 12×12 correlation matrix.

Results for the two realizations of Pop 1 and Pop 2 displayed in Figure 2 are shown in Figure 3. Looking at the quasi-circular and strong environmental effects population (Pop 1, top panel), we can notice, as expected, that the correlation is close to zero for all the off-diagonal elements of the matrix (corresponding to sky maps at different frequency bins), and equal to one on the diagonal (i.e. for an auto-correlated sky map). We obtain a similar matrix considering every quasi-circular and low environ-

mental effect population. This happens because environmental coupling produces only a flattened spectrum at lower frequencies and not a correlation of the power comparing different sky maps. On the other hand if we consider Pop 2 (bottom panel), off-diagonal elements assume values higher than zero, and quite often close to unity, meaning that sky maps are correlated due to eccentric sources emitting power at different frequencies (as clearly shown in Figure 2, where two bright sources dominate the GWB). Again, similar correlation maps are found for every individual realization of model Pop 2.

4. Recovery with simulated PTA datasets.

Although results shown thus far are encouraging, they only concern the theoretical anisotropy of the expected GWB power. In a real PTA detection, each individual SMBHB affects the pulses ToAs of each pulsar in the array and the reconstructed signal is a non trivial convolution of an incoherent superposition of deterministic GWs with the pulsar response function, contaminated by noise. It is therefore of paramount importance to test the performance of our technique on realistic simulated PTA datasets.

To this end, in Section 4.1 we inject the residuals produced by the SMBHB populations defined in Section 2.2 in an ideal SKA-like PTA (e.g., [Truant et al. 2025](#), and references therein), and employ a frequentist technique to reconstruct from the timing residuals the sky maps of the GW power at different frequencies (Section 4.2). As we will see, the resulting maps are way less polished compared to the theoretical ones, we therefore devise in Section 4.3 statistical metrics to identify eccentricity and discuss our results in Section 4.4.

4.1. Pulsar noise and realistic GWB injection

Our simulated array contains 200 pulsars randomly distributed on the sky, observed with a cadence of 14 days, over 30 years. For each of them, we simulate ToAs using the `libstempo` python wrapper ([Vallisneri 2020](#)) for the `Tempo2` pulsar timing package ([Hobbs et al. 2006](#); [Edwards et al. 2006](#)). ToA sets corresponding to the common PTA observing frequencies of 1400 and 2200 MHz are generated for each pulsar. To obtain a reasonably realistic datasets which can be analyzed rapidly enough to allow for several hundred realizations, we inject only white noise (WN) into the GW-perturbed ToAs, deferring a full analysis incorporating red noise (RN) and dispersion measure (DM) variation linked noise processes (see e.g., [Lentati et al. 2013](#); [van Haasteren et al. 2009](#)) to future work. WN appears in the timing residuals with the same power at all frequencies, thus with a flat PSD, which we model as a Gaussian random process. For standard PTA analyses, WN is composed of two terms: Error-scaling FACTor (EFAC, E_F) and Error in QUADrature (EQUAD, E_Q). The former is a multiplicative parameter that scales the ToA uncertainties to account for mis-estimation of the ToA error-bars, while the latter adds in quadrature additional noises generated for example by instrumental effects or pulse profile ‘jitter’ (see [Verbiest & Shaifullah 2018](#), and references therein). Therefore, the ToA uncertainty can be written as:

$$\sigma = \sqrt{E_F^2 \sigma_{\text{ToA}}^2 + E_Q^2}, \quad (19)$$

where σ_{ToA} is the error on the ToA. We inject WN with identical statistical properties in all pulsars, with $\sigma_{\text{ToA}} = 30$ ns, EFAC = 1.0 and EQUAD = 10^{-9} . The full set-up of the simulated PTA settings is given in Table 2.

| Settings | SKA-like PTA |
|-------------------------|----------------|
| Number of pulsars | 200 |
| T | 30 yrs |
| Cadence | 14 days |
| EFAC | 1 |
| EQUAD | 10^{-9} |
| σ_{ToA} | 30 ns |
| Observation frequencies | 1400, 2200 MHz |

Table 2: Settings of the simulated PTA used in our analysis.

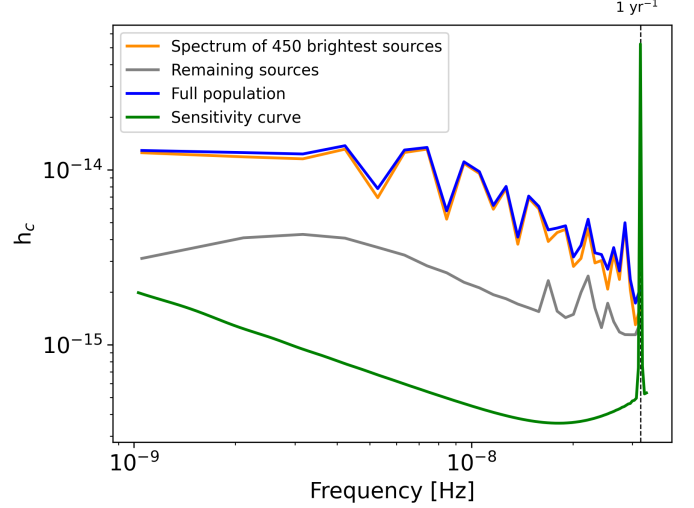


Fig. 4: GWB strain of a selected eccentric population injected in the PTA. The orange line is the total spectrum of the brightest sources injected individually. The gray line is the GWB spectrum of the remaining sources, which we have injected separately using the pipeline `fakepta` to ensure isotropy, and the blue line is the sum of the gray and orange lines. The green line marks the sensitivity of the simulated PTA.

We then add to the ToAs the GW signal generated by the SMBHB populations described in Section 2.2. Specifically, using a python and fortran based pipeline we injected in the time domain the residuals induced by each SMBHB on the ToAs of each pulsar in the PTA. In short, the code takes the initial parameters of the binary (assumed to be those at the start of observations), and it evolves it forward for the observation time T and backwards for 20000 yrs using the Post Newtonian equations of ([Barack & Cutler 2004](#)). The eccentric residuals are then injected following [Taylor et al. \(2015\)](#) and [Truant et al. \(2025\)](#), both for the Earth and the Pulsar term. The latter is computed at a time $\tau_p = -(d_p/c)(1 - \mathbf{n} \cdot \mathbf{n}_p)$, where d_p is the distance to the pulsar and \mathbf{n}, \mathbf{n}_p are the unit vectors pointing to the GW source and to the pulsar respectively. In practice we ‘rewind’ the waveform for a time τ_p and inject the corresponding chunk in the residuals. To execute this procedure we need to complement each SMBHB entry of the catalog with additional parameters, namely cosine of inclination angle, polarization, and phase. These parameters are randomly sampled within their appropriate boundaries.

Using this procedure, we create 100 mock realizations of PTA observation, for each SMBHB population model, Pop 1 and Pop 2. We note that the injected GWB in each realization has spectral properties that closely match the recovered amplitude and powerlaw spectral index from [Agazie et al. \(2024\)](#).

To speed up the dataset generation, especially for populations with high eccentricity, we made the following approximations. Since the GWB anisotropy is dominated by the loudest sources, while fainter sources make up a more isotropic background, we only individually inject the signals of the 30 brightest sources in each of the first 15 frequency bins (450 sources in total, instead of the $\approx 10^5$ SMBHB making up the overall population) and model the remaining sources as an isotropic GWB. To strain of the latter is computed at each frequency following Eq. (17), and then converted in power spectral density by applying Eq. (1). This power is then injected isotropically using a dedicated pipeline⁴.

An example of this procedure is shown in Figure 4. It is clear that the GW signal produced by the subset of the loudest SMBHBs accounts for more than 90% of the GW power, providing an excellent approximation of the properties and peculiar features of the complete population, while the remaining sources contribute to a much lower level. To ensure that this method does not bias our results, for few selected realizations, we compared resulting sky maps and correlation matrices to those obtained by injecting individually each SMBHB in the population, finding no significant difference.

4.2. Frequentist GWB power reconstruction

We now need to extract the GWB signal and its power distribution across the sky from the PTA data. Since current Bayesian pipelines for inference on the anisotropy coefficients C_ℓ are computationally demanding, requiring a large number of samples to reach convergence, in this analysis we use a more computationally efficient frequentist approach. In particular, we use the per-frequency Optimal Statistic (PFOS) tools developed by Gersbach et al. (2025)⁵ to model the GWB power, compute the C_ℓ values at the multipoles in the range $[0, \ell_{max}]$ at different GW frequencies, and consequently compute the weighted correlation \tilde{r}^{ij} as Eq. (10).

While in the “standard” OS (Anholm et al. 2009), cross-correlations between pulsars are filtered against a powerlaw GWB spectral template, PFOS has the flexibility to accept any spectral shape. It is therefore well suited for realistic GWBs, where source discreteness, eccentricity and environmental coupling can result in complex spectra. However, we note that the PFOS relies on the assumption that the signal is stationary, which breaks down in case of eccentric binaries (Falxa et al. 2024). We therefore recognize that constructing sky maps with the PFOS might be suboptimal and other techniques should be explored in the future.

According to the PFOS we can write the spatial cross-correlations between pulsars a and b at frequency f_j and their uncertainties as:

$$\rho_{ab}(f_j) = \frac{\mathbf{X}_a^T \tilde{\phi}(f_j) \mathbf{X}_b}{\text{tr}[\mathbf{Z}_a \tilde{\phi}(f_j) \mathbf{Z}_b \Phi(f_j)]}, \quad (20)$$

$$\sigma_{ab,0}(f_j)^2 = \frac{\text{tr}[\mathbf{Z}_a \tilde{\phi}(f_j) \mathbf{Z}_b \tilde{\phi}]}{\text{tr}[\mathbf{Z}_a \tilde{\phi}(f_j) \mathbf{Z}_b \Phi(f_j)]^2} \quad (21)$$

where:

$$\mathbf{X}_a = \mathbf{F}_a^T \mathbf{N}_a^{-1} \delta \mathbf{t}_a \quad \mathbf{Z}_a = \mathbf{F}_a^T \mathbf{N}_a^{-1} \mathbf{F}_a \quad (22)$$

If we collect N_r residual for pulsar a and model J frequency bins (i.e. $j = 1, 2, \dots, J$), then \mathbf{F}_a is the $N_r \times 2J$ Fourier design matrix for pulsar a , \mathbf{N}_a its diagonal $N_r \times N_r$ white noise covariance matrix and $\delta \mathbf{t}_a$ is the vector of N_r timing residuals, such that \mathbf{X}_a is a $2J$ vector and \mathbf{Z}_a is a $2J \times 2J$ matrix. $\Phi(f_j) = \phi/S(f_j)$ is the normalized Fourier domain covariance matrix, being $\phi = \phi_{j,j'} = \delta_{j,j'} S(f_j) \Delta f$. Finally, the authors introduced a new quantity $\tilde{\phi}(f_j)$ which is a frequency-selector matrix (see Pol et al. 2022; Gersbach et al. 2025, for full details).

If we divide the sky in N_{pix} equal-area pixels $\hat{\Omega}_k$ the response function of each pulsar pair in the PTA to the GW power coming from a given pixel can be written as (Pol et al. 2022):

$$R_{ab}(\hat{\Omega}_k) = \frac{3}{2} \left[\mathcal{F}_{a,j}^+(\hat{\Omega}_k) \mathcal{F}_{b,j}^+(\hat{\Omega}_k) + \mathcal{F}_{a,j}^\times(\hat{\Omega}_k) \mathcal{F}_{b,j}^\times(\hat{\Omega}_k) \right], \quad (23)$$

such that the expectation value of the normalized cross-correlation defined by Eq. (20) takes the form

$$\langle \rho_{ab}(f_j) \rangle = \Gamma_{ab}(f_j) = \sum_k P(\hat{\Omega}_k, f_j) R_{ab}(\hat{\Omega}_k), \quad (24)$$

where $P(\hat{\Omega}_k, f_j)$ is the GW signal power falling within the k -th pixel at frequency f_j . We can sum over pulsar pairs and write Eq.(24) in matricial form as $\Gamma_j = \mathbf{R} \mathbf{P}_j$, where \mathbf{P}_j is a vector of length N_{pix} defining the GW power at each pixel and \mathbf{R} is a $N_{cc} \times N_{pix}$ overlap response matrix where $N_{cc} = N_{psr}(N_{psr} - 1)/2$ is the total number of cross-correlations.

Assuming a stationary Gaussian distribution for the cross-correlation uncertainties, we can write the likelihood function for the cross-correlation vector ρ_j as:

$$p(\rho_j | \mathbf{P}_j) = \frac{\exp \left[-\frac{1}{2} (\rho_j - \mathbf{R} \mathbf{P}_j)^T \Sigma_j^{-1} (\rho_j - \mathbf{R} \mathbf{P}_j) \right]}{\sqrt{\det(2\pi \Sigma_j)}} \quad (25)$$

where Σ_j is the $N_{cc} \times N_{cc}$ noise covariance matrix of the cross-correlations at frequency f_j and ρ_j is the vector of N_{cc} cross-correlations given by Eq. (20) at each frequency bin.

In Eq. (25), we write each term $P(\hat{\Omega}_k, f_j)$ in the power matrix \mathbf{P}_j as a decomposition in square root spherical harmonics according to Eq. (4). Therefore, by maximizing the likelihood, we get an estimate of the $b_{LM}(f_j)$ coefficients from the PTA dataset, obtaining the GWB power $P_{\text{sqrt}}(\hat{\Omega}, f_j)^{1/2}$. Finally, we use this decomposition to build sky maps⁶ that we cross-correlated according to Section 2.1 to construct the correlation matrix \tilde{r}^{ij} . Following Pol et al. (2022), we compute the maximum-likelihood solution numerically using the LMFIT package (Newville et al. 2021).

Eq. (25) can also be evaluated by forcing a constant $P(\hat{\Omega}_k, f_j) = P(f_j)_{\text{iso}}$ across the sky, i.e., assuming the signal is isotropic. We can then adopt as a detection statistic for anisotropy at each frequency the signal-to-noise ratio (S/N) defined as

$$\text{S/N}_j = \sqrt{2 \ln \left[\frac{p(\rho_j | \mathbf{P}_j)}{p(\rho_j | \mathbf{P}_{j,\text{iso}})} \right]} \quad (26)$$

where we compare for each frequency bin the maximum likelihood of the recovered anisotropic sky map \mathbf{P}_j with an isotropic model $\mathbf{P}_{j,\text{iso}}$, considered as the null hypothesis. We find that in all our populations, this S/N is above 10 in the lowest frequency bin.

⁶ See notes in <https://github.com/NihanPol/MAPS>

⁴ <https://github.com/mfalxa/fakepta>
⁵ <https://github.com/GersbachKa/defiant>

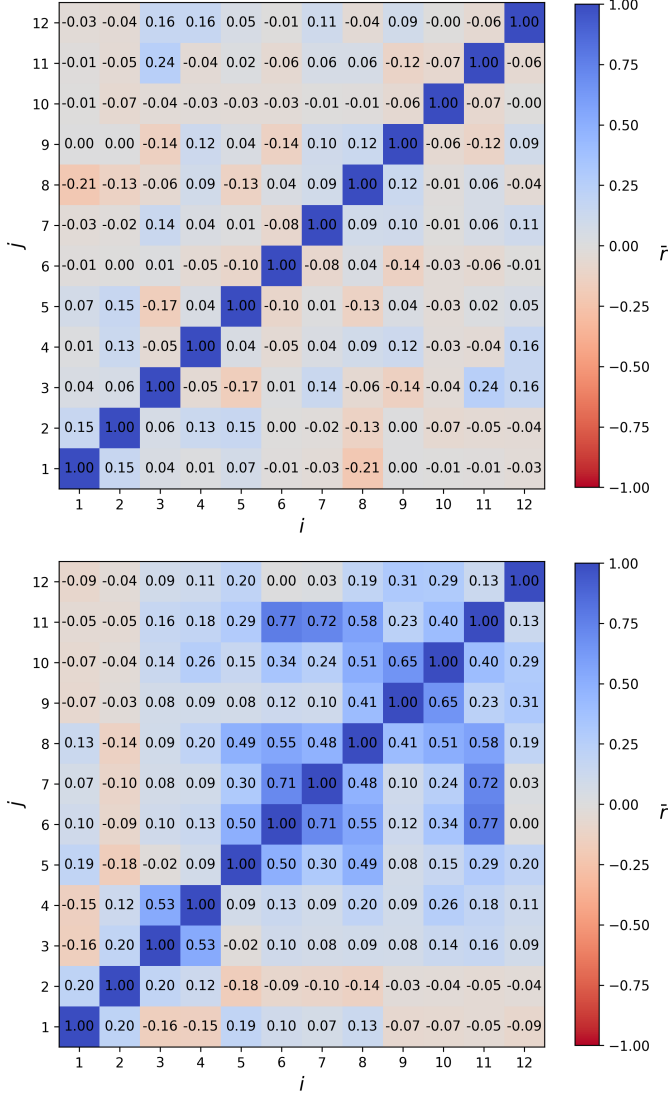


Fig. 5: Weighted correlation \bar{r}^{ij} from a single realization of Pop 1 (top panel) and Pop 2 (bottom panel) computed from the simulated PTA dataset. The color scale tracks the \bar{r}^{ij} values, which are also reported in each cell of the matrix. The i and j indices correspond to different frequency bins.

4.3. Detection statistic for eccentricity

Here, we quantify the detectability of eccentricity from sky map cross-correlation. To this end, we build a statistic to contrast the correlation matrix, \bar{r}^{ij} , of Eq. (10) produced by a population of circular binaries (Pop 1, our null hypothesis) to that generated by the eccentric population Pop 2. We proceed as follows:

1. We compute the matrix \bar{r}^{ij} for 100 independent realizations of our PTA experiment injecting SMBHBs from the Pop 1 model, and we combine the 6600 cross-correlation values (considering that \bar{r}^{ij} is a 12×12 matrix, there are $12 \times 11/2 = 66$ per realization) to construct a single correlation distribution $p(\bar{r})$ under the null hypothesis (i.e. quasi circular binaries).
2. From this, we construct the null hypothesis cross-correlation cumulative distribution $\gamma(\bar{r}) = \int_{-1}^{\bar{r}} p(r) dr$.

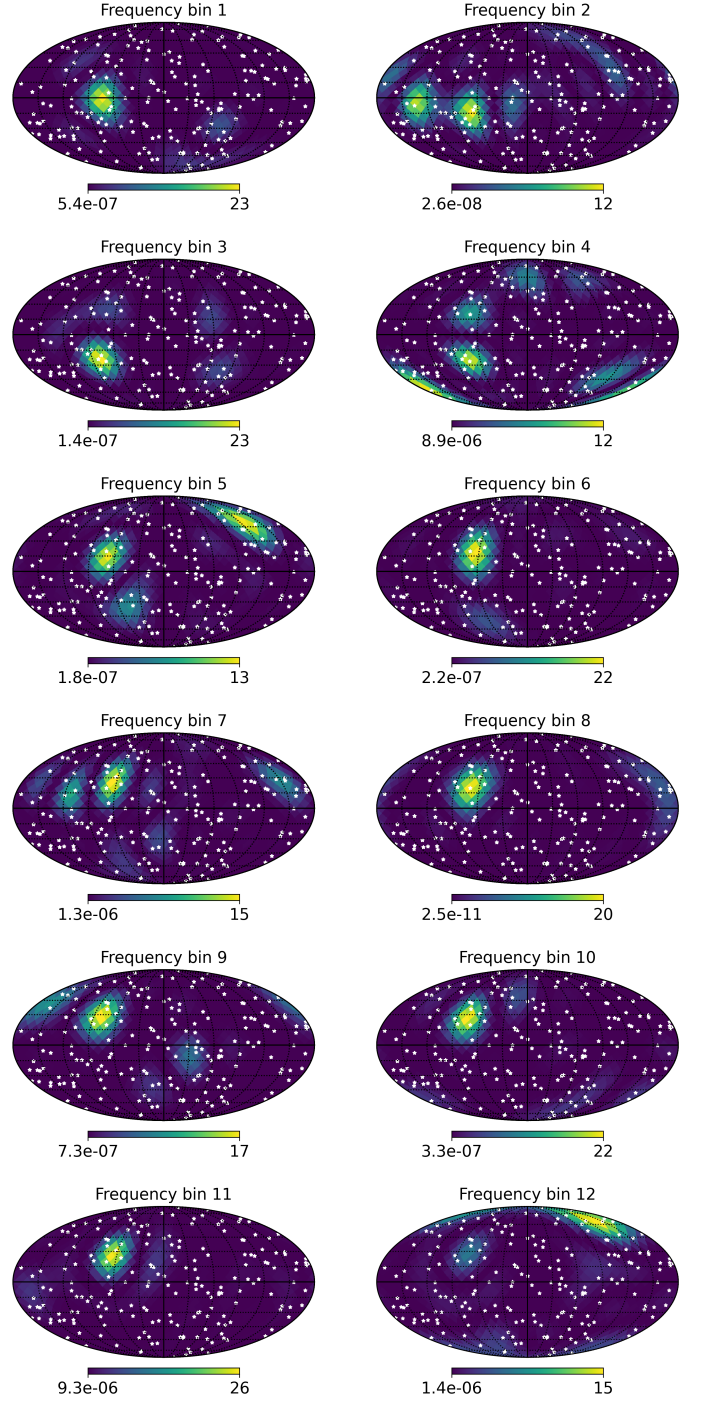


Fig. 6: Sky maps of the GWB power distribution $P(\hat{\Omega}, f_j)$ recovered from simulated PTA datasets injecting one Pop 2 realization. White stars are 200 pulsars randomly distributed in the sky. We show that in almost all frequency bins, our pipeline identifies the correct location of the two brightest sources; the first one dominates the first 4 sky maps, and the second dominates up to frequency bin 11.

3. We use the following quantity as a proxy for estimating the probability of drawing 66 values \bar{r}_k from the null hypothesis distribution:

$$\Lambda = \prod_{k=1}^{66} [1 - \gamma(\bar{r}_k)]. \quad (27)$$

4. We calculate the probability distribution of Λ in the null hypothesis $p(\Lambda_{\text{circ}})$ by drawing 8 million times 66 correlation values from the null distribution $p(\bar{r})$ and we define the significance at which the null hypothesis can be rejected given a measured likelihood Λ (i.e. p -value) as:

$$S = \int_{-\infty}^{\Lambda} p(\Lambda_{\text{circ}}) \quad (28)$$

5. Finally, we calculate the correlation matrix \bar{r}^{ij} for 100 PTA experiments featuring Pop 2 in the injection and, for each of them, compute the likelihood Λ_{ecc} of extracting the 66 reconstructed \bar{r}^{ij} correlation values from the null correlation distribution according to Eq. (27).

If the correlation matrices of Pop 2 are significantly different from those derived under the null hypothesis (Pop 1), the obtained values of Λ_{ecc} will fall in the tail of the distribution $p(\Lambda_{\text{circ}})$, and the null hypothesis can be rejected with high significance. We note that, by computing a single $p(\bar{r})$ in step 1, we are implicitly assuming that all individual \bar{r}^{ij} follow the same distribution in the null hypothesis. We verified that this is the case by testing each $p(\bar{r}^{ij})$ distribution against the overall $p(\bar{r})$ one with a Kolmogorov-Smirnov test, finding no significant outliers.

4.3.1. Triplets

The statistic defined in the previous section is only based on the values of the \bar{r}^{ij} correlation coefficients, regardless of their location in the correlation matrix. This latter, however, bears information about the nature of the signal, since eccentric binaries are expected to be more strongly correlated in adjacent frequency bins. This is due to the smooth shape of the function $g(n, e)$, which features an e -dependent peak at some n . In a first attempt to account for the expected larger correlation in adjacent frequency bins, we construct a coefficient $C(i, j, j+1)$ capturing the correlation of the sky map at frequency f_i with two sky maps at frequencies f_j, f_{j+1} as:

$$C(i, j, j+1) = \bar{r}^{ij} + \bar{r}^{i, j+1} + \bar{r}^{j, j+1}. \quad (29)$$

Using 12 frequency bins, we can construct 100 of these sky map correlation coefficient ‘triplets’ instead of the 66 \bar{r}^{ij} . To test whether this triplet correlation can better identify eccentricity, we construct a ‘triplets’ detection statistic following steps 1 to 5 of the previous section but starting from $C(i, j, j+1)$ instead of \bar{r}^{ij} .

4.4. Results

In Figure 5 we show correlation matrices obtained from the PFOS presented in Section 4.2 for the same SMBHB populations shown in Figure 3. For Pop 1, we get what we expected: diagonal values equal to one and off-diagonal elements close to zero. Looking at Pop 2, we still recover correlations in off-diagonal elements, even though we notice that values are lower than the theoretical ones shown in Figure 3 (see Section 5 for more details). Despite this, we still recognize that two eccentric bright sources dominate the GWB, producing correlations in different sky maps.

Those are evident in Figure 6, where we show that we can reconstruct the sky localization of these sources in almost all frequency bins, although with larger uncertainties and additional hot spots compared to Figure 2 (right panels).

The poorer quality of the reconstructed sky maps results in less distinctive correlation values for the circular and eccentric SMBHB populations, as shown in Figure 7. While for Pop 1 there is virtually no difference in the distribution $p(\bar{r}^{ij})$ whether it is calculated from the theoretical sky maps of h_c^2 or it is reconstructed from a realistic PTA (orange histograms), this is not the case for Pop 2 (green histograms). The $p(\bar{r}^{ij})$ reconstructed from the PTA, while presenting a significant tail at positive correlation values, is identical null hypothesis distribution.

To quantify the detectability of eccentricity we then compute the correlation pairs and triplets statistics described in the previous section, testing 100 realizations of PTAs featuring a Pop 2 injection. Results are shown in Figure 8, where we compare the likelihood of these 100 eccentric models against the null hypothesis. For the correlation pair statistic (left panel) we observe that the Λ_{ecc} distribution is much more skewed towards lower value but we get a p -value $S < 1.4 \times 10^{-3}$ (i.e. a 3σ rejection of the null hypothesis) only in 37% of cases. The same threshold is surpassed in 52% of the cases for triplets statistic (right panel), which indeed, by including the correlation of multiple adjacent bins, performs better.

5. Discussion and conclusions

We developed a method to detect a correlated GW sky power distribution across the frequency spectrum by cross-correlating sky maps at different frequencies. This is particularly interesting because such correlations arise if the GWB present in the data is generated by a population of eccentric binaries that emit power across a broad frequency spectrum. Our method can therefore be used to distinguish a GWB produced by a quasi-circular SMBHB population affected by environmental coupling from one generated by an eccentric population of SMBHBs featuring similar spectral attenuation at low frequencies. We demonstrated the key concept by constructing the cross-correlation matrix of theoretical sky maps of the GW power only and then tested its validity on realistic (although highly idealized) PTA datasets.

Although the method performs flawlessly on theoretical maps, it is less effective (yet still valuable) on simulated data. This is because the reconstructed sky maps are much less precise, leading to correlation matrices that are less informative than the theoretical ones, as highlighted in Figure 7.

There are multiple reasons contributing to this lower performance.

1. The PTA observable is an incoherent superposition of GWs with different initial phases in the time domain. When multiple GWs of comparable amplitude contribute to the overall power, their inherent incoherency is likely to wash out correlations, resulting in smaller values of \bar{r}^{ij} . Although this is certainly a limiting factor, it does not seem to be a no-go for real-life applications of this technique. In fact, we found that our correlation statistics perform much better when increasing the number of pulsars in the array from 100 to 200.
2. An additional limiting factor is given by the size and properties of the adopted PTAs. Intrinsic noise, complicated and broad response functions and sparse distribution of the pulsars all contribute to the degradation of the reconstruction of the sky distribution of the GW power.
3. Another real-life complication that requires further investigation is the occurrence of leakage, as can be observed in Figure 6 where we occasionally recover sky maps that are offset compared to the theoretical ones. In fact, in frequency bins 8 and 11, we recover the sky position of the second

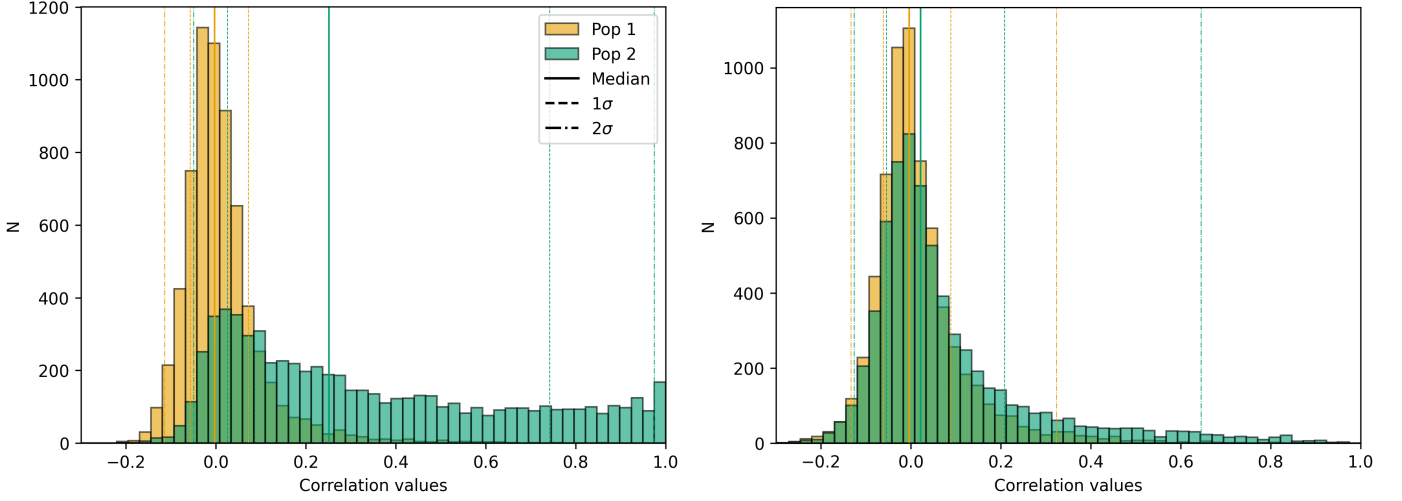


Fig. 7: Correlation distributions of Pop 1 and Pop 2 realizations recovered from known SMBHB (left plot), and from simulated PTA datasets (right plot).

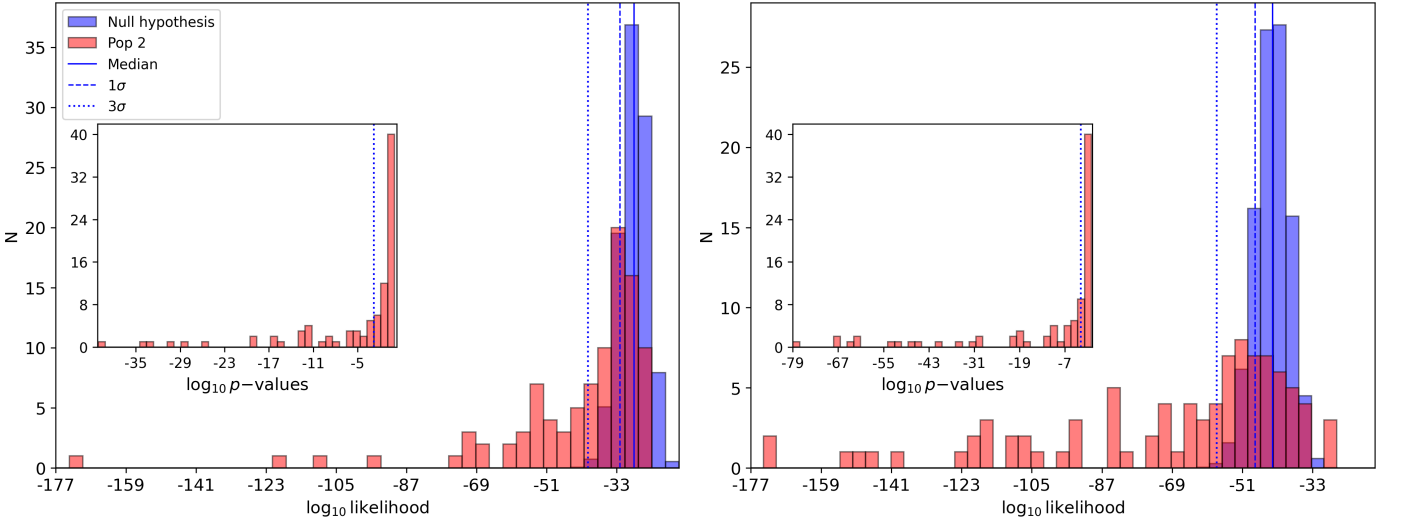


Fig. 8: Likelihood distributions of Pop 2 realizations compared to the null hypothesis using pair (left plot) and triplet correlations (right plot). Note that 3 and 6 realizations of Pop 2 (in left and right plots, respectively) are not shown because their likelihood values are equal to zero, which implies strong correlation. The p -value distributions are also shown in the inset plots. There, 3 and 13 realizations of Pop 2 which have p -values equal to zero do not appear in the left and right plots, respectively.

brightest source, even though none of its harmonics fall in those bins, and another fainter source should dominate the GW power. This could be due to power leakage occurring when a loud harmonic falls at the edge of two frequency bins.

4. Lastly, to construct the sky maps, we used the frequentist PFOS outside of its strict validity domain. In fact, in the presence of eccentric binaries, the GWB is non-stationary and the PFOS (as most PTA analysis tools) is not strictly applicable since the Fourier domain covariance matrix of the GWB is not diagonal. Although we showed that reconstructed sky maps are reasonable (cf Figure 6), more sophisticated reconstruction techniques need to be developed.

We also caution that the SMBHB populations employed in this initial investigation were simplistic, featuring binaries all sharing the same eccentricity at formation, $e_0 = 0.01$ for Pop 1 and $e_0 = 0.9$ for Pop 2. Since anisotropies in the GWB power

distribution are generally dominated by a few loud sources, the detection of correlation mostly constrains the properties of those loud systems, which might not be representative of the overall population. In an extreme (likely unrealistic) example, strong correlation might be detected even if a single loud eccentric source dominates the GW power emitted by a population of otherwise circular binaries. We defer tests involving more complex SMBHB populations to future work.

With anisotropy studies like this, we can constrain the sky position of multiple single sources, as well as the strain $h_c(f)$ given the computed power at different frequency bins. Thus, this method is complementary to the Bayesian/Frequentist Continuous Gravitational Waves (CGW) searches that use a circular and eccentric pipeline (e.g., [Bécsy et al. 2022](#); [Ferranti et al. 2025](#), and references therein). Moreover, through anisotropy studies, we can put constraints on the prior range of CGW searches, reducing the parameter space and the computation time, increas-

ing the possibility to constrain other CGW parameters. Future projects will involve multiple CGW searches and comparing results with anisotropy studies.

To conclude, we developed and tested this new analysis using a simulated PTA dataset, enabling the recovery of the expected correlation using eccentric and quasi-circular populations applying the PFOS tools. This method also allows us to recover the sky localization of the bright sources that dominate the GWB. Work is currently in progress to improve the pipeline and make it applicable to real PTA datasets.

Acknowledgements. We thank the B-Massive group at Milano-Bicocca University for useful discussions and comments. B.E.M, A.S, G.M.S, D.I.V, and A.C acknowledge the financial support provided under the European Union's H2020 ERC Consolidator Grant "Binary Massive Black Hole Astrophysics" (B Massive, Grant Agreement: 818691) and the financial support provided under the European Union Advanced Grant "PINGU" (Grant Agreement: 101142079). AC acknowledges financial support from the European Research Council (ERC) starting grant 'GIGA' (grant agreement number: 101116134). LS would like to acknowledge the support of the European Space Agency through ESA's postdoctoral Research Fellowship programme.

References

- Agazie, G., Antoniadis, J., Anumalapudi, A., et al. 2024, *ApJ*, 966, 105
- Agazie, G., Anumalapudi, A., Archibald, A. M., et al. 2023, *ApJ*, 951, L50
- Agazie, G., Anumalapudi, A., Archibald, A. M., et al. 2023a, The NANOGrav 15-year Data Set: Search for Anisotropy in the Gravitational-Wave Background
- Agazie, G. et al. 2023b, *The Astrophysical Journal Letters*, 951, L8
- Allen, B., Agarwal, D., Romano, J. D., & Valtolina, S. 2024, *Physical Review D*, 110
- Amaro-Seoane, P., Sesana, A., Hoffman, L., et al. 2010, *MNRAS*, 402, 2308
- Anholm, M., Ballmer, S., Creighton, J. D. E., Price, L. R., & Siemens, X. 2009, *Phys. Rev. D*, 79, 084030
- Antoniadis, J., Arumugam, P., Arumugam, S., et al. 2024, *Å*, 690, A118
- Antoniadis, J. et al. 2023, *Å*, 678, A50
- Barack, L. & Cutler, C. 2004, *Phys. Rev. D*, 69, 082005
- Bartolo, N., Matarrese, S., Riotto, A., & Väihkönen, A. 2007, *Phys. Rev. D*, 76, 061302
- Boyle, L. A. & Buonanno, A. 2008, *Phys. Rev. D*, 78, 043531
- Bundy, K., Fukugita, M., Ellis, R. S., et al. 2009, *The Astrophysical Journal*, 697, 1369
- Bécsy, B., Cornish, N. J., & Digman, M. C. 2022, *Physical Review D*, 105
- Bécsy, B., Cornish, N. J., Meyers, P. M., et al. 2023, *The Astrophysical Journal*, 959, 9
- Bécsy, B., Cornish, N. J., Petrov, P., et al. 2025, Towards robust gravitational wave detections from individual supermassive black hole binaries
- Cusin, G., Pitrou, C., Pijenburg, M., & Sesana, A. 2025, Measuring anisotropies in the PTA band with cross-correlations
- Damour, T. & Vilenkin, A. 2000, *Phys. Rev. Lett.*, 85, 3761
- Depta, P. F., Domcke, V., Franciolini, G., & Pironi, M. 2024, Pulsar timing array sensitivity to anisotropies in the gravitational wave background
- Edwards, R. T., Hobbs, G. B., & Manchester, R. N. 2006, *Monthly Notices of the Royal Astronomical Society*, 372, 1549
- Ellis, J. A., Vallisneri, M., Taylor, S. R., & Baker, P. T. 2019, ENTERPRISE: Enhanced Numerical Toolbox Enabling a Robust Pulsar Inference Suite, Astrophysics Source Code Library, record ascl:1912.015
- Falxa, M., Leclerc, H. Q., & Sesana, A. 2024, From eccentric binaries to nonstationary gravitational wave backgrounds
- Ferranti, I., Shaifullah, G., Chalumeau, A., & Sesana, A. 2025, *Å*, 694, A194
- Gair, J., Romano, J. D., Taylor, S., & Mingarelli, C. M. 2014, *Physical Review D*, 90
- Gardiner, E. C., Kelley, L. Z., Lemke, A.-M., & Mitridate, A. 2024, Beyond the Background: Gravitational Wave Anisotropy and Continuous Waves from Supermassive Black Hole Binaries
- Gersbach, K. A., Taylor, S. R., Meyers, P. M., & Romano, J. D. 2025, *Phys. Rev. D*, 111, 023027
- Grimm, N., Pijenburg, M., Cusin, G., & Bonvin, C. 2025, *Journal of Cosmology and Astroparticle Physics*, 2025, 011
- Grunthal, K., Nathan, R. S., Thrane, E., et al. 2024, *Monthly Notices of the Royal Astronomical Society*, 536, 1501–1517
- Hellings, R. W. & Downs, G. S. 1983, *ApJ*, 265, L39
- Hindmarsh, M., Huber, S. J., Rummukainen, K., & Weir, D. J. 2014, *Phys. Rev. Lett.*, 112, 041301
- Hiramatsu, T., Kawasaki, M., & Saikawa, K. 2014, *J. Cosmology Astropart. Phys.*, 2014, 031
- Hobbs, G., Edwards, R., & Manchester, R. 2006, *Chinese Journal of Astronomy and Astrophysics Supplement*, 6, 189
- Jaffe, A. H. & Backer, D. C. 2003, *ApJ*, 583, 616
- Kelley, L. Z., Blecha, L., Hernquist, L., Sesana, A., & Taylor, S. R. 2017, *MNRAS*, 471, 4508
- Kormendy, J. & Ho, L. C. 2013, *ARA&A*, 51, 511
- Kosowsky, A., Turner, M. S., & Watkins, R. 1992, *Phys. Rev. D*, 45, 4514
- Lemke, A.-M., Mitridate, A., & Gersbach, K. A. 2024, Detecting Gravitational Wave Anisotropies from Supermassive Black Hole Binaries
- Lentati, L., Alexander, P., Hobson, M. P., et al. 2013, *Phys. Rev. D*, 87, 104021
- Lotz, J. M., Jonsson, P., Cox, T. J., & Primack, J. R. 2010, *MNRAS*, 404, 575
- Matarrese, S., Pantano, O., & Saez, D. 1993, *Phys. Rev. D*, 47, 1311
- Miles, M. T., Shannon, R. M., Reardon, D. J., et al. 2024, *Monthly Notices of the Royal Astronomical Society*, stae2571
- Mingarelli, C. M. F., Lazio, T. J. W., Sesana, A., et al. 2017, *Nature Astronomy*, 1, 886–892
- Mingarelli, C. M. F., Sidery, T., Mandel, I., & Vecchio, A. 2013, *Physical Review D*, 88
- Newville, M., Otten, R., Nelson, A., et al. 2021, *lmfit/lmfit-py: 1.0.3*
- Peters, P. C. & Mathews, J. 1963, *Physical Review*, 131, 435
- Phinney, E. S. 2001, *arXiv e-prints*, astro
- Pol, N., Taylor, S. R., & Romano, J. D. 2022, *ApJ*, 940, 173
- Rajagopal, M. & Romani, R. W. 1995, *ApJ*, 446, 543
- Ravi, V., Wyithe, J. S. B., Hobbs, G., et al. 2012, *ApJ*, 761, 84
- Ravi, V., Wyithe, J. S. B., Shannon, R. M., Hobbs, G., & Manchester, R. N. 2014, *MNRAS*, 442, 56
- Reardon, D. J., Zic, A., et al. 2023, *The Astrophysical Journal Letters*, 951, L6
- Romano, J. D. & Cornish, N. J. 2017, *Living Reviews in Relativity*, 20, 2
- Rosado, P. A., Sesana, A., & Gair, J. 2015, *MNRAS*, 451, 2417
- Sah, M. R., Maurya, A., Mukherjee, S., et al. 2025 [arXiv:2505.22745]
- Sah, M. R., Mukherjee, S., Saeedzadeh, V., et al. 2024, *Monthly Notices of the Royal Astronomical Society*, 533, 1568–1582
- Sampson, L., Cornish, N. J., & McWilliams, S. T. 2015, *Phys. Rev. D*, 91, 084055
- Sato-Polito, G. & Kamionkowski, M. 2023, Exploring the spectrum of stochastic gravitational-wave anisotropies with pulsar timing arrays
- Semenzato, F., Casey-Clyde, J. A., Mingarelli, C. M. F., et al. 2024, Cross-Correlating the Universe: The Gravitational Wave Background and Large-Scale Structure
- Sesana, A. 2010, *ApJ*, 719, 851
- Sesana, A. 2013, *Classical and Quantum Gravity*, 30, 224014
- Sesana, A., Haardt, F., & Madau, P. 2006, *ApJ*, 651, 392
- Sesana, A., Vecchio, A., & Colacino, C. N. 2008, *MNRAS*, 390, 192
- Sesana, A., Vecchio, A., & Volonteri, M. 2009, *MNRAS*, 394, 2255
- Sorbo, L. 2011, *J. Cosmology Astropart. Phys.*, 2011, 003
- Taylor, S. R. & Gair, J. R. 2013, *Physical Review D*, 88
- Taylor, S. R., Mingarelli, C. M. F., Gair, J. R., et al. 2015, *Phys. Rev. Lett.*, 115, 041101
- Taylor, S. R., van Haasteren, R., & Sesana, A. 2020, *Phys. Rev. D*, 102, 084039
- Tomczak, A. R., Quadri, R. F., Tran, K.-V. H., et al. 2014, *ApJ*, 783, 85
- Tomita, K. 1967, *Progress of Theoretical Physics*, 37, 831
- Truant, R. J., Izquierdo-Villalba, D., Sesana, A., Shaifullah, G. M., & Bonetti, M. 2025, *Å*, 694, A282
- Vallisneri, M. 2020, libstempo: Python wrapper for Tempo2, Astrophysics Source Code Library, record ascl:2002.017
- Valtolina, S., Shaifullah, G., Samajdar, A., & Sesana, A. 2024, *Å*, 683, A201
- van Haasteren, R., Levin, Y., McDonald, P., & Lu, T. 2009, *MNRAS*, 395, 1005
- Verbiest, J. P. W. & Shaifullah, G. M. 2018, *Classical and Quantum Gravity*, 35, 133001
- Wyithe, J. S. B. & Loeb, A. 2003, *ApJ*, 590, 691
- Xu, H., Chen, S., et al. 2023, *Research in Astronomy and Astrophysics*, 23, 075024
- Zonca, A., Singer, L., Lenz, D., et al. 2019, *Journal of Open Source Software*, 4, 1298
- Ölmez, S., Mandic, V., & Siemens, X. 2012, *Journal of Cosmology and Astroparticle Physics*, 2012, 009–009